

Ponderings on the Possible Preponderance of Perpendicular Planets

JARED C. SIEGEL ^{1,*} JOSHUA N. WINN ¹ AND SIMON H. ALBRECHT ^{2,1}

¹*Department of Astrophysical Sciences, Princeton University, 4 Ivy Lane, Princeton, NJ 08544, USA*

²*Stellar Astrophysics Centre, Department of Physics and Astronomy, Aarhus University, Ny Munkegade 120, 8000 Aarhus C, Denmark*

ABSTRACT

Misalignments between planetary orbits and the equatorial planes of their host stars are clues about the formation and evolution of planetary systems. Earlier work found evidence for a peak near 90° in the distribution of stellar obliquities, based on frequentist tests. We performed hierarchical Bayesian inference on a sample of 174 planets for which either the full three-dimensional stellar obliquity has been measured (72 planets) or for which only the sky-projected stellar obliquity has been measured (102 planets). We investigated whether the obliquities are best described by a Rayleigh distribution, or by a mixture of a Rayleigh distribution representing well-aligned systems and a different distribution representing misaligned systems. The mixture models are strongly favored over the single-component distribution. For the misaligned component, we tried an isotropic distribution and a distribution peaked at 90°, and found the evidence to be essentially the same for both models. Thus, our Bayesian inference engine did not find strong evidence favoring a “perpendicular peak,” unlike the frequentist tests. We also investigated selection biases that affect the inferred obliquity distribution, such as the bias of the gravity-darkening method against obliquities near 0° or 180°. Further progress in characterizing the obliquity distribution will probably require the construction of a more homogeneous and complete sample of measurements.

1. INTRODUCTION

A planet’s orbital motion is not necessarily aligned with its host star’s rotation. The degree of misalignment is quantified by the obliquity, ψ , defined as the angle between the direction \hat{n}_* of the star’s rotational angular momentum and the direction \hat{n}_o of the planet’s orbital angular momentum. Measurements of the obliquity or its sky-projection, λ , have been performed for several hundred transiting exoplanets (see [Triaud 2018](#); [Albrecht et al. 2022](#), for reviews).

It is hoped that such measurements will help us understand the processes of planet formation and post-formation dynamical interactions. For example, the observation that hot Jupiters around low-mass stars tend to have low obliquities has been interpreted as the outcome of tidal dissipation within the star ([Winn et al. 2010](#)), while observations of high obliquities have been variously attributed to planet-planet scattering, Von

Zeipel–Kozai–Lidov cycles, and other mechanisms (see Section 4 of [Albrecht et al. 2022](#)). In a few cases, there are enough clues available to implicate a particular obliquity-excitation mechanism; for example, in the K2-290 system, there is evidence that a companion star was responsible for tilting the protoplanetary disk ([Hjorth et al. 2021](#)). Drawing population level conclusions will require knowledge of the statistical distribution of stellar obliquities and its dependence on the characteristics of planetary systems and their host stars.

Modeling of the obliquity distribution has been undertaken by [Fabrycky & Winn \(2009\)](#), [Morton & Winn \(2014\)](#), [Mazeh et al. \(2015\)](#), [Winn et al. \(2017\)](#), [Muñoz & Perets \(2018\)](#), and [Louden et al. \(2021\)](#), using different techniques and progressively larger samples. In general, investigators have modeled the distribution as a mixture of a well-aligned component and a very broad component, and have shown evidence that the broad component consists preferentially of “hot” stars (with masses between 1.2 and 1.9 M_\odot and effective temperatures between 6200 and 8000 K).

Importantly, most of the measurement techniques are not capable of determining ψ directly, but are instead sensitive to either the sky-projected obliquity (λ) or the

Corresponding author: Jared Siegel
siegeljc@princeton.edu

* NSF Graduate Research Fellow

difference between the line-of-sight inclinations of the spin and orbital axes (i_* and i_o). The various angles are related via the equation

$$\hat{n}_* \cdot \hat{n}_o = \cos \psi = \cos i_* \cos i_o + \sin i_* \sin i_o \cos \lambda. \quad (1)$$

Recently, [Albrecht et al. \(2021\)](#) assembled a sample of systems for which constraints on λ , i_o , and i_* are all available, usually because more than one measurement technique was applied to the same system. In this sample, the misaligned component of the obliquity distribution appeared to have a broad peak at 80 – 125° , rather than falling off smoothly from 0° or extending all the way to 180° . Frequentist tests assigned low probabilities ($p \lesssim 10^{-3}$) to the hypothesis that the peak is a statistical fluke, given the null hypothesis of isotropy.

The motivation for the work described in this paper was to (i) repeat the frequentist tests now that more data points have been obtained, (ii) compare different models for the obliquity distribution using Bayesian hierarchical modeling, and (iii) investigate selection effects that might influence the results. This paper is organized as follows. Section 2 describes the available sample. Section 3 revisits the frequentist tests of [Albrecht et al. \(2021\)](#), and Section 4 outlines the Bayesian modeling framework. The results are presented in Section 5. In addition to analyzing the entire sample, we examined subsamples that are expected to be influenced by tides, or for which tides should be negligible, as described in Section 6. Selection biases are investigated in Section 7. Our conclusions are summarized in Section 9.

2. SAMPLE

[Albrecht et al. \(2022\)](#) compiled a catalog of planets for which measurements of the sky-projected obliquity λ are available, a subset of which also have measurements of the full-obliquity ψ . We supplemented this catalog with 16 newly available measurements (Table 1), of which 12 are for systems that previously lacked any obliquity measurements, and 4 are for systems that now have full-obliquity information where only the projected-obliquity measurement was previously available. The combined catalog consists of 174 planets. Of these, 72 planets have measurements of both λ and i_* ; we will refer to these 72 planets as the ψ sample. For the other 102 planets, λ has been measured but there are no available constraints on i_* ; we will refer to these planets as the λ sample. Figure 1 displays some key properties of the ψ and λ samples.

Most of the λ measurements were obtained by observing the Rossiter-McLaughlin effect, and most of the i_* information comes from the combination of measurements of projected rotation velocity $v \sin i$, rotation period, and stellar radius ([Masuda & Winn 2020](#)).

Table 1. Extension of the [Albrecht et al. \(2022\)](#) sample of projected-obliquity λ and obliquity ψ measurements.

Name	λ [deg]	ψ [deg]	Update	Ref.
55 Cnc e	$10.0^{+17.0}_{-20.0}$	$23.0^{+14.0}_{-12.0}$	—	1
HAT-P-3 b	21.2 ± 8.7	$75.7^{+8.5}_{-7.9}$	✓	2
HAT-P-33 b	5.9 ± 4.1	—	—	2
HAT-P-49 b	97.7 ± 1.8	—	—	2
HD 3167 b	$6.6^{+6.6}_{-7.9}$	$29.5^{+7.2}_{-9.4}$	✓	3
HD 3167 c	$108.9^{+5.4}_{-5.5}$	$107.7^{+5.1}_{-4.9}$	✓	3
HD 89345 b	$74.2^{+33.6}_{-32.5}$	$80.1^{+22.3}_{-23.1}$	—	2
HIP 41378 d	$57.1^{+26.4}_{-17.9}$	—	—	4
K2-105 b	$81.0^{+50.0}_{-47.0}$	—	—	2
KELT-11 b	$77.86^{+2.36}_{-2.26}$	—	—	5
Qatar-6 A b	0.1 ± 2.6	$21.82^{+8.86}_{-18.36}$	—	6
TOI-1478 b	$6.2^{+5.9}_{-5.5}$	—	—	7
TOI-2076 b	$3.0^{+16.0}_{-15.0}$	$18.0^{+10.0}_{-9.0}$	—	8
TOI-640 b	176.0 ± 3.0	104.0 ± 2.0	—	9
WASP-156 b	$105.7^{+14.0}_{-14.4}$	—	—	2
WASP-47 b	0.0 ± 24.0	$29.2^{+11.1}_{-13.3}$	✓	2

NOTE—A check mark in the “Update” column indicates a planet that appeared in the [Albrecht et al. \(2022\)](#) catalog for which updated measurements are now available. References: 1 ([Zhao et al. 2022](#)), 2 ([Bourrier et al. 2023](#)), 3 ([Bourrier et al. 2021](#)), 4 ([Grouffal et al. 2022](#)), 5 ([Mounzer et al. 2022](#)), 6 ([Rice et al. 2023](#)), 7 ([Rice et al. 2022](#)), 8 ([Frazier et al. 2022](#)), 9 ([Knudstrup et al. 2023](#)).

For KELT-9, KELT-17, Kepler-13, MASCARA-4, and WASP-189 the obliquity was inferred from the gravity-darkening method. For HAT-P-7 and HD 89345, the stellar inclination was constrained via asteroseismology.

3. FREQUENTIST HYPOTHESIS TESTING

[Albrecht et al. \(2021\)](#) noted an apparent concentration of obliquities near 90° in the ψ sample that was available at the time. Focusing attention on the 19 planets with $\cos \psi < 0.75$ in their sample, they asked: under the null hypothesis that the spin and orbital axes are uncorrelated, how often would the distribution of ψ be concentrated near 90° as strongly as seen in the real data? The concentration was quantified by either the dispersion of $\cos \psi$ around 0 or by the standard deviation of $\cos \psi$, and in both cases the null hypothesis was rejected with $p \lesssim 10^{-3}$.

In the updated sample, 25 systems satisfy the misalignment criterion $\cos \psi < 0.75$. In each of 10^6 trials, we drew 25 values of $\cos \psi$ from the distribution $\mathcal{U}(-1, 0.75)$ representing the null hypothesis. We then drew values of $\cos \psi$ from the measurement posteriors

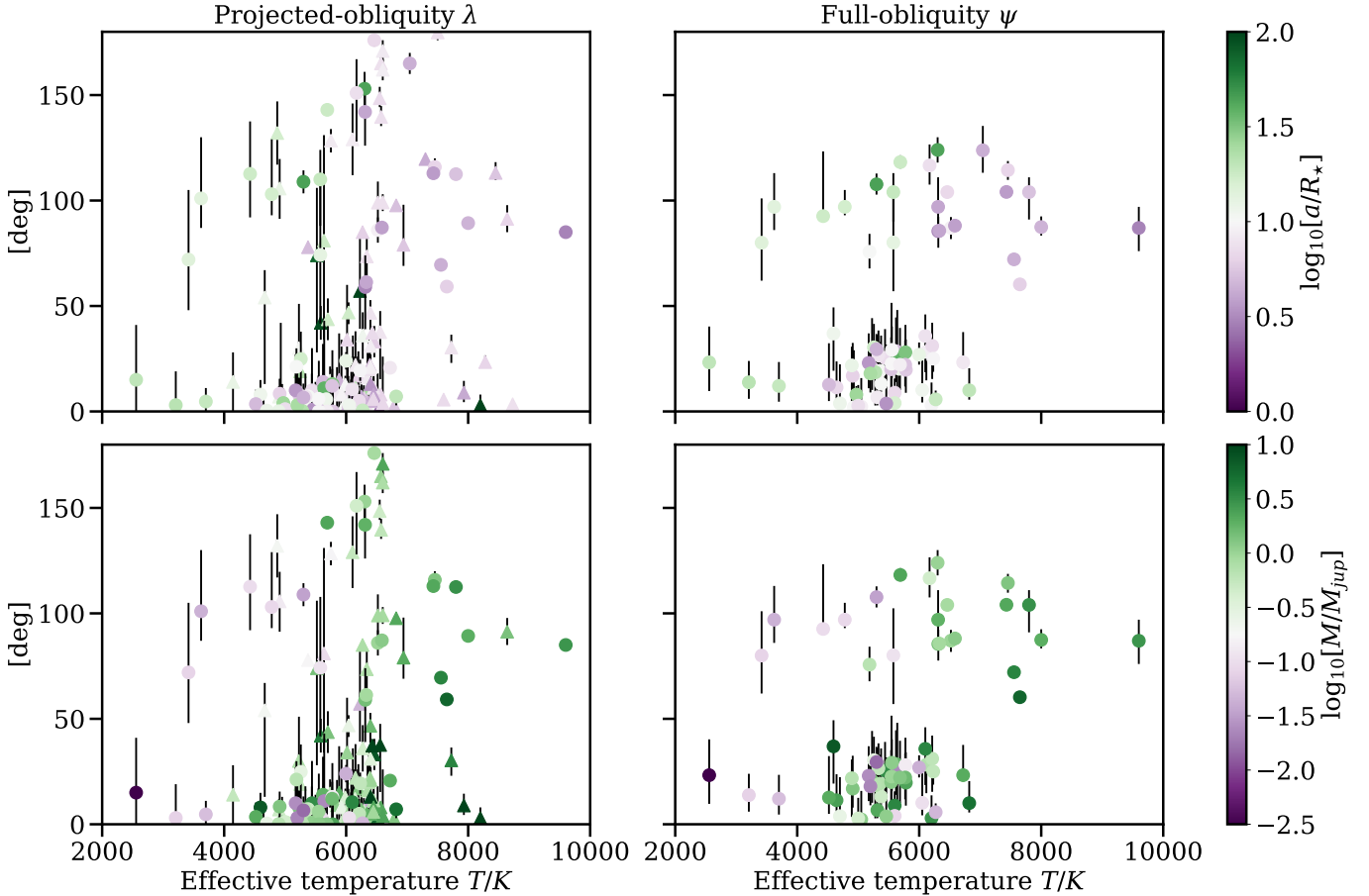


Figure 1. Planetary and stellar parameters for systems with λ measurements and the subset of systems with ψ measurements (right). In the top and bottom rows, the color of the data points conveys the planet’s orbital separation and mass, respectively. Triangular data points are members of the λ sample, i.e., λ has been measured but not ψ . Circular data points are for the ψ sample, i.e., both λ and ψ have been measured.

of the 25 systems for which $\cos \psi < 0.75$. Unlike Albrecht et al. (2021), who approximated the measurement posteriors as skew-normal distributions, we drew directly from the measurement posteriors. Using this method and the same sample as Albrecht et al. (2021), the null hypothesis was rejected with median p-values of $p = 2.5 \times 10^{-3}$ and 0.8×10^{-3} , in terms of the dispersion and standard deviation respectively. After adding the new and updated measurements, the null hypothesis was rejected with median p-values of $p = 0.5 \times 10^{-3}$ and 0.2×10^{-3} . Thus, regardless of whether the concentration was quantified by the dispersion or standard deviation, the null hypothesis sample was rejected with high confidence, and the new data reduced the corresponding p-values by factors of 5 and 4.

As acknowledged by Albrecht et al. (2021), these frequentist tests are difficult to interpret because the tests were devised after seeing the data. Also, frequentist tests can demonstrate that the data are inconsistent with the null hypothesis, but they leave one wonder-

ing which probability distributions *are* consistent with the data. Answering the latter question was the goal of the hierarchical Bayesian modeling described below.

4. HIERARCHICAL BAYESIAN INFERENCE

4.1. Formalism

For a given dataset \vec{d} , a property of the system x can be inferred from the posterior probability distribution

$$p(x | \vec{d}) \propto p(\vec{d} | x) \pi_0(x), \quad (2)$$

where $p(\vec{d} | x)$ is the likelihood function and $\pi_0(x)$ is the prior on x . For example, \vec{d} might represent a time series of radial velocities exhibiting the Rossiter-McLaughlin effect, and x might represent λ .

In a hierarchical model, we use a collection of N datasets $\{\vec{d}_1, \dots, \vec{d}_N\}$ to infer the parameters Θ of a model for the distribution $f_x(x | \Theta)$. Assuming the datasets $\{\vec{d}_i\}$ are independent of each other, the like-

likelihood function for the model parameters is

$$\mathcal{L}(\{\vec{d}_i\} | \Theta) = \prod_{i=1}^N \int p(\vec{d}_i | x) f_x(x | \Theta) dx, \quad (3)$$

$$\propto \prod_{i=1}^N \int p(x | \vec{d}_i) \frac{f_x(x | \Theta)}{\pi_0(x)} dx. \quad (4)$$

The population distribution $f_x(x | \Theta)$ is essentially treated as a prior on x ; marginalizing over x then leaves a likelihood function for Θ . Throughout this work, the likelihood function for the model parameters is denoted $\mathcal{L}(\text{data} | \text{model})$; all other probability density functions are denoted $p(X | Y)$.

For our application, we modeled the obliquity distribution $f_{\cos \psi}(\cos \psi | \Theta)$ using different samples of planets, and different likelihood functions for each sample. The choices for the likelihood function were

- The λ likelihood, based only on measurements of λ , without any constraints on i_* .
- The ψ likelihood, based on measurements of ψ , or separate measurements of both λ and i_* .
- The ψ & λ likelihood, i.e., the combination of ψ likelihoods for systems where constraints on ψ are available, and λ likelihoods for systems for which only λ has been measured.

For the λ likelihood, the data set consists of N_λ posteriors for λ , and we relate λ and ψ using

$$\tan \lambda = \tan \psi \sin \phi, \quad (5)$$

an equation valid for $i_o \approx 90^\circ$, as is the case for transiting planets considered throughout this work. Here, ϕ is the azimuthal angle of \hat{n}_* in a spherical polar coordinate system in which \hat{n}_o is the polar axis. The azimuthal angle is assumed to be uniformly distributed, i.e.,

$$f_{\sin \phi}(x) = \frac{2}{\pi} \frac{1}{\sqrt{1-x^2}}. \quad (6)$$

The likelihood function for Θ is

$$\begin{aligned} \mathcal{L}_\lambda(\{\vec{d}_i\} | \Theta) &\propto \prod_{i=1}^{N_\lambda} \int_{\cos \psi, \sin \phi} d \cos \psi \times d \sin \phi \\ &\times p_\lambda(\tan^{-1}[\tan \psi \sin \phi] | \vec{d}_i) \\ &\times f_{\cos \psi}(\cos \psi | \Theta) \\ &\times f_{\sin \phi}(\sin \phi), \end{aligned} \quad (7)$$

where p_λ is the likelihood function for λ given \vec{d}_i , the data for the i th system. This likelihood function is made

computationally tractable via the K -samples approximation (Hogg et al. 2010):

$$\mathcal{L}_\lambda(\{\vec{d}_i\} | \Theta) \propto \prod_{i=1}^{N_\lambda} \frac{1}{K} \sum_{k=1}^K \mathcal{N}(\tan^{-1}[\tan \psi_{k,\Theta} \sin \phi_k] | \lambda_i, \sigma_{\lambda_i}), \quad (8)$$

where $\cos \psi_{k,\Theta}$ is the k th draw from $f_{\cos \psi}(\cos \psi | \Theta)$, $\sin \phi_k$ is the k th draw from $f_{\sin \phi}$, and $K = 1000$. For inference of the underlying obliquity distribution, we found it convenient to sample from the distribution $f_{\cos \psi}$ and approximate each measurement posterior as a normal distribution.

For the ψ likelihood, the details depend on the measurement technique. In most cases, there are measurement posteriors for λ , $v \sin i$, P_{rot} , and R_* , and the stellar inclination is constrained using the equation

$$\sin i = \frac{P_{\text{rot}}}{2\pi R} v \sin i, \quad (9)$$

from which the obliquity can be calculated using Equation 1. The likelihood function in this case is

$$\begin{aligned} \mathcal{L}_\psi(\{\vec{d}_i\} | \Theta) &\propto \prod_{i=1}^{N_\psi} \int_{\cos \psi, \sin \phi, v} d \cos \psi \times d \sin \phi \times dv \\ &\times p_{v \sin i}(v \cos \psi / \cos \lambda | \vec{d}_i) \\ &\times p_\lambda(\tan^{-1}[\tan \psi \sin \phi] | \vec{d}_i) \\ &\times p_v(v | \vec{d}_i) \\ &\times f_{\cos \psi}(\cos \psi | \Theta) \\ &\times f_{\sin \phi}(\sin \phi). \end{aligned} \quad (10)$$

For notational convenience, we combined the $P_{\text{rot},i}$ and $R_{*,i}$ measurements into a likelihood for the rotation velocity $p_v(v | \vec{d}_i)$. We evaluated the likelihood function via the K -samples approximation, drawing from the $f_{\cos \psi}$, $f_{\sin \phi}$, and p_v distributions.

In the cases for which the obliquity determination was based on asteroseismology or gravity darkening, we used the measurement posterior for $\cos \psi$, giving a likelihood function

$$\begin{aligned} \mathcal{L}_\psi(\{\vec{d}_i\} | \Theta) &\propto \prod_{i=1}^{N_\psi} \int_{\cos \psi} d \cos \psi \\ &\times p_{\cos \psi}(\cos \psi | \vec{d}_i) \\ &\times f_{\cos \psi}(\cos \psi | \Theta). \end{aligned} \quad (11)$$

For our K -samples approximation, we approximated the posterior for $\cos \psi$ as a normal distribution.

4.2. Models for the obliquity distribution

Four models for the obliquity distribution were considered. The models were designed to determine whether the obliquity distribution has multiple components, and if so, whether the misaligned component is peaked at a particular value. In order of increasing complexity, the models are:

0. A Rayleigh distribution for ψ with a single parameter σ_R specifying the mode and width of the distribution.
1. A mixture of a Rayleigh distribution for ψ and an isotropic distribution (uniform in $\cos \psi$). In addition to σ_R , this model has a parameter q specifying the fraction of systems that are drawn from the Rayleigh distribution.
2. A mixture of a Rayleigh distribution for ψ and an “isonormal” distribution, a function of our devising that interpolates between an isotropic distribution and a normal distribution (see Figure 2):

$$f_{\text{isonormal}}(\cos \psi \mid \mu, w) \propto w f_{\text{isotropic}}(\cos \psi) + (1 - w) \mathcal{N}\left(\cos \psi \mid \mu, \frac{w}{3}\right), \quad (12)$$

where \mathcal{N} is a normal distribution with mean μ and standard deviation $w/3$. As $w \rightarrow 0$, f_{IG} tends toward a Dirac delta function centered at μ , and as $w \rightarrow 1$, $f_{\text{isonormal}} \rightarrow f_{\text{isotropic}}$. For this model, μ is held fixed at 0 (the “perpendicular preponderance”) and the adjustable parameters are σ_R , q , and w .

3. The same as Model 3 but allowing the mean μ of the peaked distribution to be an adjustable parameter, for a total of four parameters: $\{\sigma_R, q, \mu, w\}$.

These models were selected because they have a minimal number of free parameters and are easy to interpret. Each model is normalized such that $\int_{-1}^1 f_{\cos \psi} d \cos \psi = 1$. We adopted the following priors on the model parameters:

$$\begin{aligned} \sigma_R &\sim \begin{cases} \mathcal{U}(0.3, 2.0 \text{ rad}) & \text{in Model 0,} \\ \mathcal{U}(\frac{\pi}{180}, 0.5 \text{ rad}) & \text{in Models 1–3,} \end{cases} \\ q &\sim \mathcal{U}(0, 1), \\ w &\sim \mathcal{U}(0, 1), \\ \mu &\sim \mathcal{U}(-0.5, 0.5). \end{aligned}$$

The lower bounds on σ_R were introduced to avoid numerical instabilities; as long as they are sufficiently small, the specific values do not materially affect the results.

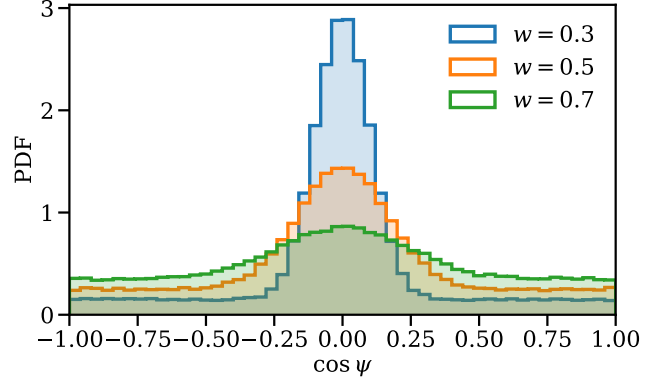


Figure 2. The isonormal distribution used in Model 2, for different choices of w .

5. BAYESIAN MODEL SELECTION

The Bayes factor (or evidence ratio) was used to evaluate the competing models. For a data set $\{\vec{d}_i\}$ and model M with free-parameters Θ , the Bayesian evidence is defined as

$$p(\{\vec{d}_i\} \mid M) = \int \mathcal{L}(\{\vec{d}_i\} \mid M, \Theta) \pi_0(\Theta) d\Theta, \quad (13)$$

where $\mathcal{L}(\{\vec{d}_i\} \mid M, \Theta)$ is the likelihood function and $\pi_0(\Theta)$ is the prior on the model parameters. The Bayesian evidence for each model was calculated via the K -samples approximation, using a number of samples equal to the number of free parameters times 10^6 . The sampling error in the calculation of the Bayesian evidence was estimated by redrawing from the Monte Carlo samples 100 times for each model.

Given two competing models M_0 and M_1 , the Bayes factor is

$$R = \frac{p(\{\vec{d}_i\} \mid M_0)}{p(\{\vec{d}_i\} \mid M_1)}. \quad (14)$$

If the prior probabilities of models M_0 and M_1 are equal, R is the ratio of the posterior probabilities for M_0 and M_1 given the data $\{\vec{d}_i\}$. In this case, a Bayes factor of $R > 1$ implies M_0 is favored over M_1 with $R : 1$ odds. Bayes factors of $R = 10, 20$, and 100 correspond to odds ratios of 91, 95, and 99%, respectively; see [Trotta \(2007\)](#) and [Abbott et al. \(2018\)](#) for reviews and applications of the Bayes factor.

5.1. Full-obliquity modeling

To begin, the evidence and the posteriors for the parameters of each obliquity distribution model were inferred using the ψ sample, i.e., the 72 planets for which information about both λ and i_* is available. Here and

Table 2. Bayes Factors R relative to Model 1

Restriction	Sample	N	Model 0	Model 2	Model 3
None	ψ	72	$(14 \pm 8) \times 10^{-20}$	2.7 ± 0.5	1.2 ± 0.2
	λ	102	$(5 \pm 2) \times 10^{-14}$	0.382 ± 0.007	0.307 ± 0.006
	ψ & λ	174	$(3 \pm 2) \times 10^{-29}$	1.1 ± 0.8	0.6 ± 0.2
No G.D.	ψ	67	$(8 \pm 6) \times 10^{-20}$	1.6 ± 0.1	0.85 ± 0.08
	λ	102	$(37 \pm 3) \times 10^{-15}$	0.377 ± 0.008	0.308 ± 0.006
	ψ & λ	169	$(3 \pm 4) \times 10^{-30}$	0.5 ± 0.1	0.4 ± 0.1
No G.D. & Giants with Weak Tides	ψ	31	$(34 \pm 1) \times 10^{-8}$	1.08 ± 0.03	0.69 ± 0.02
	λ	70	$(42 \pm 2) \times 10^{-10}$	0.74 ± 0.01	0.434 ± 0.006
	ψ & λ	101	$(76 \pm 10) \times 10^{-15}$	0.84 ± 0.03	0.53 ± 0.02

NOTE—G.D. is gravity darkening. R is the ratio of the models' posterior probabilities, given the data and assuming equal prior probabilities. $R > 1$ implies M_i is favored over M_1 with $R : 1$ odds.

Table 3. Parameters of the model obliquity distributions, based on complete measurement samples.

Sample		ψ	λ	ψ & λ
N		72	102	174
Model 0	σ_R [deg]	44^{+3}_{-3}	42^{+3}_{-3}	42^{+3}_{-3}
Model 1	σ_R [deg]	$2.0^{+0.9}_{-0.6}$	9^{+3}_{-2}	5^{+1}_{-1}
	q	$0.55^{+0.05}_{-0.05}$	$0.65^{+0.06}_{-0.06}$	$0.58^{+0.04}_{-0.03}$
Model 2	σ_R [deg]	$2.1^{+1.0}_{-0.6}$	10^{+3}_{-3}	5^{+1}_{-1}
	q	$0.58^{+0.05}_{-0.06}$	$0.67^{+0.06}_{-0.06}$	$0.6^{+0.04}_{-0.04}$
	w	$0.7^{+0.2}_{-0.1}$	$0.8^{+0.1}_{-0.2}$	$0.8^{+0.1}_{-0.1}$
Model 3	σ_R [deg]	$2.1^{+1.0}_{-0.6}$	10^{+3}_{-3}	5^{+1}_{-1}
	q	$0.6^{+0.06}_{-0.06}$	$0.66^{+0.06}_{-0.07}$	$0.59^{+0.06}_{-0.04}$
	w	$0.7^{+0.2}_{-0.2}$	$0.8^{+0.1}_{-0.2}$	$0.83^{+0.09}_{-0.12}$
	μ	$0.0^{+0.2}_{-0.2}$	$0.0^{+0.3}_{-0.3}$	$0.0^{+0.3}_{-0.2}$

NOTE— Parameter posteriors for each combination of model (e.g., 0, 1, 2, or 3) and type of data (ψ collection, λ collection, and the ψ & λ collection). The reported posteriors are the 16, 50, and 84th percentiles.

in the other cases described below, the posteriors for the model parameters were inferred with a Markov Chain Monte Carlo method, using 40 walkers for 50,000 iterations, of which the first third were discarded as burn-in (a conservative threshold based on visual convergence of the walker chains). Table 2 gives the Bayes factors relative to Model 1, and Table 3 gives the 16, 50, and 84th percentiles of the posteriors of the model parameters.

In Model 0 (Rayleigh), the width σ_R was found to be $44^\circ \pm 3^\circ$. This model was strongly disfavored ($R < 10^{-9}$) relative to the other models in which the misaligned systems were described by a separate component. We con-

Table 4. Parameters of the model obliquity distributions, based on giant planets with weak tides and removing the gravity darkening measurements.

Sample		ψ	λ	ψ & λ
N		31	70	101
Model 0	σ_R [deg]	50^{+6}_{-5}	40^{+3}_{-3}	43^{+3}_{-3}
Model 1	σ_R [deg]	$2.1^{+1.7}_{-0.8}$	13^{+3}_{-3}	8^{+2}_{-2}
	q	$0.43^{+0.08}_{-0.08}$	$0.69^{+0.07}_{-0.08}$	$0.56^{+0.06}_{-0.06}$
Model 2	σ_R [deg]	$2.2^{+2.1}_{-0.9}$	14^{+3}_{-3}	9^{+3}_{-2}
	q	$0.45^{+0.08}_{-0.08}$	$0.73^{+0.07}_{-0.07}$	$0.59^{+0.06}_{-0.06}$
	w	$0.7^{+0.2}_{-0.2}$	$0.7^{+0.2}_{-0.2}$	$0.7^{+0.2}_{-0.2}$
Model 3	σ_R [deg]	$2.1^{+2.0}_{-0.8}$	14^{+3}_{-3}	8^{+3}_{-2}
	q	$0.45^{+0.08}_{-0.08}$	$0.71^{+0.07}_{-0.08}$	$0.58^{+0.06}_{-0.06}$
	w	$0.7^{+0.2}_{-0.2}$	$0.8^{+0.2}_{-0.2}$	$0.8^{+0.1}_{-0.2}$
	μ	$0.1^{+0.2}_{-0.3}$	$0.0^{+0.3}_{-0.2}$	$0.1^{+0.2}_{-0.2}$

NOTE— Parameter posteriors for each combination of model (e.g., 0, 1, 2, or 3) and type of data (ψ collection, λ collection, and the ψ & λ collection). The reported posteriors are the 16, 50, and 84th percentiles.

clude that the obliquity distribution is best described as a mixture between a well-aligned component and a misaligned component, rather than a single smooth distribution.

In the multi-component models (1–3), the fraction of systems belonging to the Rayleigh component was $\approx 60\%$, and σ_R was found to be $\approx 2^\circ$. Regarding the misaligned components, the Bayesian evidence favors the peaked models (2 and 3) over the isotropic distribution (1), but not significantly. Model 2 (Rayleigh + 90° peak) is favored over Model 1 (Rayleigh + isotropic)

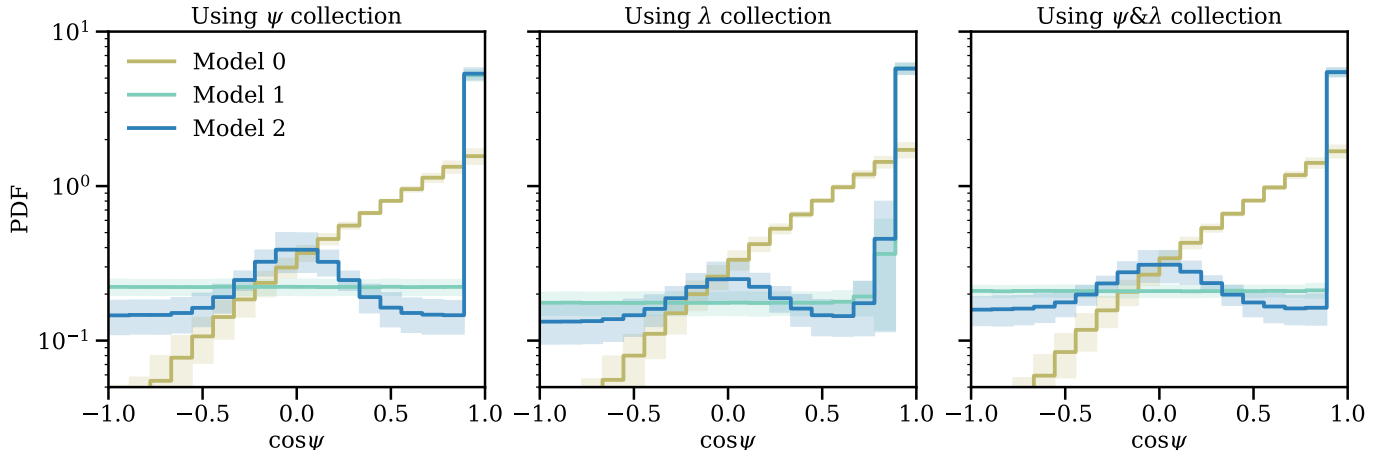


Figure 3. Inferred obliquity distributions for different samples and likelihoods. Regardless of the sample, the peak in the isonormal model is small enough to be consistent or nearly consistent with the isotropic model. Left: The ψ sample of 72 planets for which measurements of both λ and i_* are available, analyzed with the ψ likelihoods. Center: The λ sample of 102 planets, analyzed with the λ likelihoods. Right: The entire ψ & λ sample of 174 planets, analyzed with the ψ & λ likelihoods. Solid lines demarcate the mean, and the shaded regions show the 1σ uncertainty intervals.

with $R \approx 3$. Model 3, in which the peak location is allowed to vary, is consistent with a peak at 90° ; however, the constraint on μ is weak and the degree of concentration is low. For Models 2–3, the width parameter w was found to be $\gtrsim 0.7$, indicating a broad distribution. The inferred obliquity distributions are visualized in Figure 3.

For reference, we repeated the inference using the same sample of 72 planets, but using only the λ likelihoods and ignoring the constraints on the stellar inclination angle. The results are nearly the same as those that were obtained using the ψ likelihoods, all consistent within 1σ . Evidently, the inclination information has only a minor effect on the results.¹

5.2. Projected-obliquity modeling

Next, we considered the λ sample, consisting of 102 planets for which only λ was measured and no information is available about the stellar inclination. Table 2 gives the Bayes factors relative to Model 1, and Table 3 gives the 16, 50, and 84th percentiles of the model posteriors. The inferred obliquity distributions are visualized in Figure 3.

Again, Model 0 (Rayleigh) was strongly disfavored relative to the multi-component models. Also similar to the previous case is that Models 1–3 were found to be effectively indistinguishable by the Bayesian evidence; Model 1 is favored with odds ratios ≈ 3 . In Models 2–3, the width parameter w was found to be $0.8^{+0.1}_{-0.2}$. Rela-

tive to the ψ sample, the λ sample favors a larger width for the well-aligned component ($\sigma_R \approx 10^\circ$ compared to $\sigma_R \approx 2^\circ$) and provides weaker evidence for models with a peaked misaligned component; these trends may indicate underlying differences between the ψ and λ sample, which we investigate in Section 7.

5.3. Joint obliquity and projected-obliquity modeling

Finally, we took advantage of all the available information. We combined the collection of ψ constraints from the 72 systems in the ψ sample with the λ constraints from the 102 systems in the λ sample. The Bayes factors relative to Model 1 are presented in Table 2. Table 3 presents the 16, 50, and 84th percentiles of the model posteriors. The inferred obliquity distributions are visualized in Figure 3. Model 0 was strongly disfavored relative to Models 1–3, and Models 1–3 were effectively indistinguishable. The preferred models are a mixture of a narrow Rayleigh distribution and a very broad or isotropic component.

To summarize, the single-component Model 0 was always trounced by the multi-component Models 1–3. While the results of analyzing the ψ and λ systems differ in detail, neither the isotropic model nor the peaked models were strongly favored by the Bayesian evidence.

6. SAMPLE DEPENDENCE

The sample of planets covers a wide range of orbital separations, planet masses, and stellar types. The resulting diversity of possible modes of planet formation and evolution makes the obliquity distribution of the entire sample difficult to interpret. In particular, for massive close-orbiting planets, dissipative tidal interactions

¹ This conclusion was also reached by Dong & Foreman-Mackey in work shared with us prior to publication.

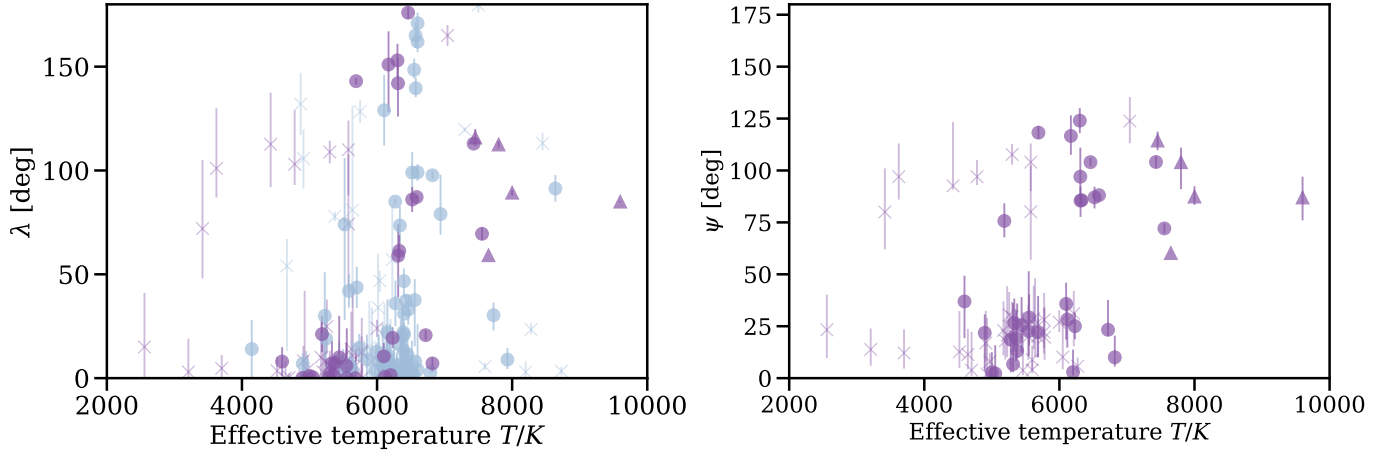


Figure 4. Projected-obliquity (left) and full-obliquity (right) versus stellar effective temperature. Blue points represent planets for which λ has been measured but not ψ . Purple points represent planets for which ψ has been measured. Circles are the giant-planet hosts in the weak-tides sample, triangles are the gravity-darkening measurements, and crosses are all other measurements.

generally lead to orbital circularization, synchronization of spin and orbital periods, and spin-orbit alignment. Tidal dissipation is expected to be faster for low-mass host stars with thick convective envelopes (with effective temperatures below the “Kraft break” at about 6250 K) than for more massive stars with radiative envelopes. Although the mechanism by which tidal dissipation occurs is uncertain, the obliquity data shows the qualitative trends one would expect from tidal dissipation. Close-orbiting giant planets around low-mass stars generally have low obliquities, while a broader distribution of obliquities is seen in systems with smaller planets, wider orbits, or hotter stars (Winn et al. 2010; Albrecht et al. 2012, 2022).

In an effort to simplify the interpretation of the obliquity distribution, we repeated our Bayesian model comparisons after applying restrictions to the samples intended to group together systems where one might expect similar formation mechanisms and obliquity-altering mechanisms to have occurred. We focused on giant planets ($M_p > 0.3M_{\text{Jup}}$), and included those with $a/R_\star < 300$ (a criterion that excluded only β Pic b). We omitted the 5 systems for which the obliquity was determined with the gravity darkening method, out of concern about a selection bias favoring large misalignments (see Section 7.4). For a system to be categorized as having “weak tides”, we required $a/R_\star > 7$ or $T_{\text{eff}} < 6250$ K. Figure 4 shows key properties of the samples and identifies the weak-tides systems.

6.1. Weak tides

After applying the weak-tides restriction, the λ sample consists of 70 giant planets for which only the projected obliquity has been measured, and the ψ sample consists

of 31 giant planets for which full-obliquity information is available. Because tidal dissipation is expected to be negligible, the obliquity distribution inferred for these samples may more closely reflect the outcome of the formation and migration mechanisms.

As in Section 5, the parameters were inferred for 4 different models for the obliquity distribution, and different choices for the sample and likelihood function. Table 4 gives the credible intervals of the parameters of the models for the obliquity distribution.

The results of analyzing the weak-tides sample were largely consistent with the results of analyzing the unrestricted sample. We expected the weak-tides sample to give a lower value of q , the fraction of systems in the well-aligned Rayleigh component, and a larger value of σ_R , the scale factor of the well-aligned component, but these differences did not emerge at a statistically significant level. Instead, discrepancies arose between the model posteriors inferred from the λ and ψ samples. Relative to the ψ sample, the λ sample favored a larger width for the well-aligned component ($\sigma_R \approx 10^\circ$ vs. 2°) and a higher fraction of well-aligned planets ($q \approx 0.7$ vs. 0.5).

Table 2 gives the Bayes factor of each model (relative to Model 1) for samples with weak tides. Regardless of the sample and likelihoods that were used, the single Rayleigh distribution was strongly disfavored relative to the multi-component models, and the multi-component models were supported by nearly equivalent evidence.

6.2. Strong tides

We also constructed a sample of giant planets for which tides are expected to be strong, using the criteria $M_p > 0.3M_{\text{Jup}}$, $a/R_\star > 7$, and $T_{\text{eff}} < 6250$ K. After ap-

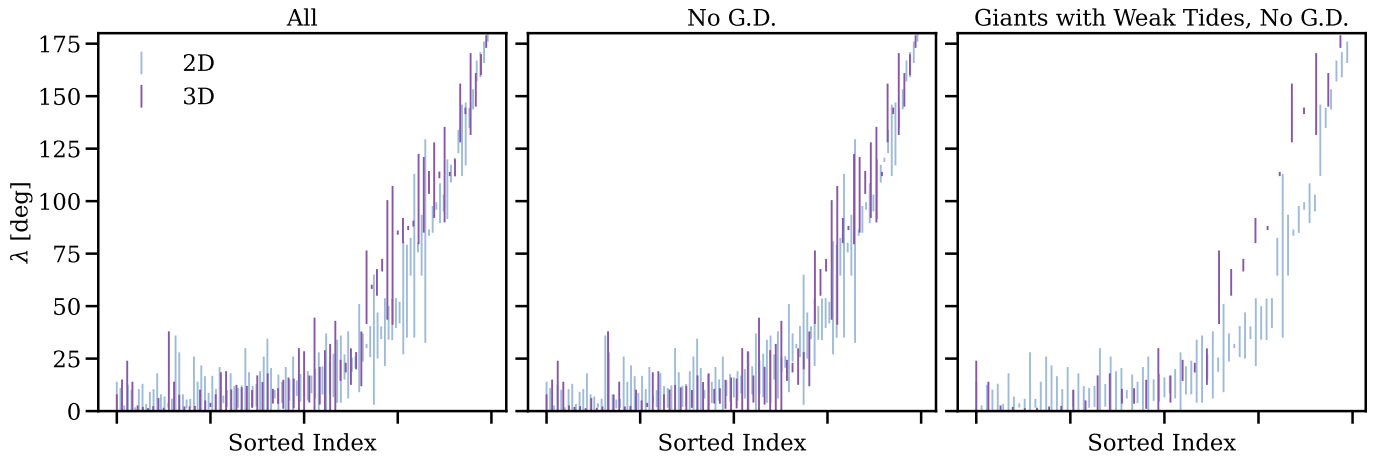


Figure 5. The λ measurements from the ψ sample are slightly but systematically higher than the λ measurements from the λ sample. This effect is likely due at least in part to the selection bias of the gravity darkening method, which was used in 5 cases in the ψ sample and no cases in the λ sample. In each panel, the λ measurements are plotted from lowest to highest, with blue points for the λ sample and purple points for the ψ sample. The left panel shows all available measurements. The center panel omits data from the gravity darkening method. The right panel is for the weak-tides sample. For each measurement, the 1σ uncertainty interval is plotted as a vertical line.

plying these restrictions, the ψ sample has 11 members and the λ sample has 12 members. These systems might be expected to have systematically low obliquities due to tidal obliquity damping, and indeed, the data are all consistent with zero obliquity, with varying degrees of uncertainty.

For this sample, the multi-component models are unjustified, and only Model 0 was fitted. For the three choices of sample and likelihood (ψ , λ , and ψ & λ), the Rayleigh scale factor was found to be 4_{-2}^{+3} , 5_{-2}^{+4} , and $4_{-2}^{+2}[\circ]$, respectively. The 95th percentile upper bounds on the Rayleigh scale factor are 9, 11, and $7[\circ]$, respectively.

7. SELECTION BIASES

The frequentist tests of the ψ sample assigned a low probability to an isotropic distribution for the misaligned systems, and our Bayesian analysis of the ψ sample gave somewhat stronger evidence for a 90° peak than an isotropic distribution. Yet, our analysis of the λ sample favored an isotropic distribution. Additionally, the posterior distributions of the model parameters only partially overlapped between the ψ and λ samples. Although the Bayes factors were modest in all cases, we wondered how and why the ψ sample might differ from the λ sample. Figure 5 shows the projected-obliquity measurements from the λ sample alongside those from the ψ sample. In this figure, the λ measurements in the ψ sample appear to be systematically higher than those in the λ sample.

This made us question some premises implicit in all of the work described above, namely, that the planets

with full-obliquity information are drawn randomly from the same parent population as the planets with only projected-obliquity information, and that the availability of full-obliquity information is independent of the value of the obliquity. In this section, we consider the possibility that these premises are false. Below, in Section 7.1, we describe some statistical tests, and in Sections 7.2, 7.3, and 7.4, we discuss some possible sources of bias inherent in the measurement techniques.

7.1. Observational evidence

To test the null hypothesis that the stellar obliquities in the ψ and λ samples are drawn from the same distribution, we applied the Kolmogorov-Smirnov (KS) test in a series of 1,000 Monte Carlo trials. For a given trial, we drew (with replacement) N_ψ values of λ from the ψ sample, and N_λ values of λ from the λ sample. These values were drawn from the measurement posteriors for each system. Then, the two-sample KS test was applied to compute the p -value for the null hypothesis that the λ values are drawn from the same distribution. The null hypothesis was “ruled out” ($p < 5\%$) in $\lesssim 5\%$ of the trials. This was true when the method was applied to the entire planet sample, and when it was applied after enforcing either the weak-tides or strong-tides restrictions. Two-sample Anderson-Darling tests also ruled out the null hypothesis in $\lesssim 5\%$ of the trials, for each choice of sub-sample. The median p -value was 50% for the whole sample and 40% for the tidally-decoupled sample. Thus, these tests did not reject the hypothesis that the λ measurements in the ψ sample are drawn from the same distribution as the λ measurements in the λ sample.

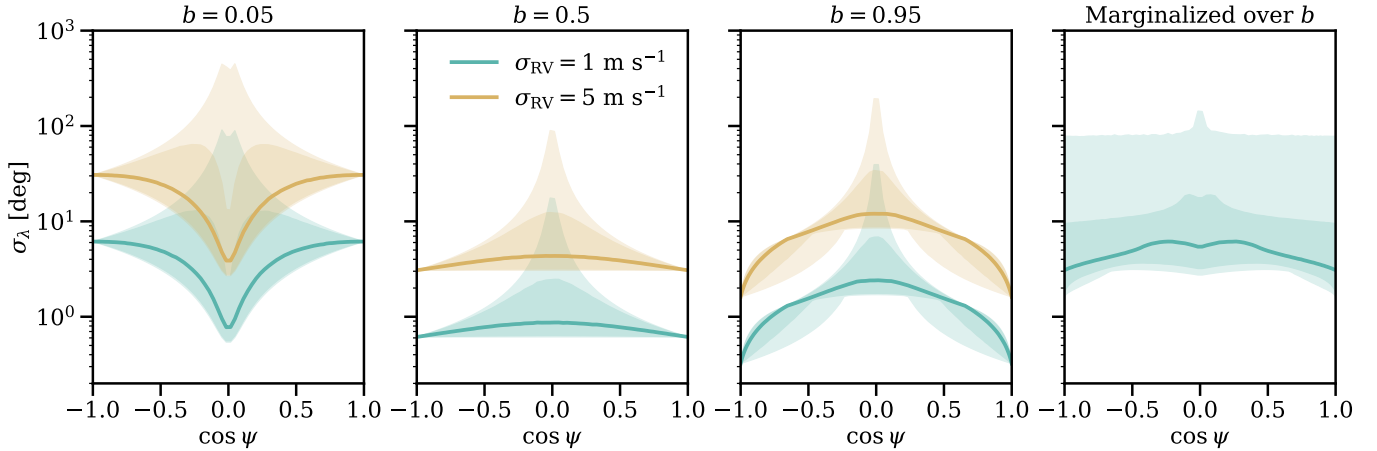


Figure 6. The distribution of achievable measurement precision in λ for the nominal system described in the text, assuming random stellar orientations and either a fixed impact parameter or a uniform distribution of impact parameters. The median value of σ_λ is presented as a solid line, and the shaded regions demarcate the 1σ and 2σ percentiles. Color indicates the assumed radial velocity measurement uncertainty: 1 m s^{-1} (blue) or 5 m s^{-1} (gold).

7.2. Rossiter-McLaughlin effect

For most of the systems in the ψ sample, λ was measured with the Rossiter-McLaughlin (RM) effect and i_\star was measured or constrained with a different method. The RM effect, in brief, is the distortion of a star’s spectral lines that occurs during transits due to stellar rotation. For example, when a planet blocks a portion of the approaching half of the stellar disk, the blueshifted components of the spectral lines are slightly suppressed, which can be detected directly in the line profile or as an apparent redshift of the entire line. This “anomalous” Doppler shift depends chiefly on $v \sin i$, λ , the transit depth $\delta \approx (r/R)^2$, and the transit impact parameter b . Gaudi & Winn (2007) derived an approximate formula, later corrected by Albrecht et al. (2022), for the achievable uncertainty in λ as a function of the system parameters:

$$\sigma_\lambda = \frac{\sigma_v/\sqrt{N}}{v \sin i} \left(\frac{r}{R}\right)^{-2} \left[\frac{(1-b^2) \cos^2 \lambda + 3b^2 \sin^2 \lambda}{b^2(1-b^2)} \right]^{1/2}. \quad (15)$$

The derivation assumes there are N uniformly spaced radial velocity measurements, each with an uncertainty of σ_v . Limb darkening is neglected, as are the uncertainties in b and r/R .

The dependence of σ_λ on λ raises the question of whether the sample of systems with published obliquity measurements is biased in favor of obliquities that tend to allow for smaller values of σ_λ and consequently higher probabilities to detect the RM effect. To understand this source of bias, we conducted a series of Monte Carlo trials involving a hypothetical $1 R_\odot$ star with rotation velocity $v = 2.5 \text{ km s}^{-1}$ and a transiting Jupiter-sized

planet. In each trial, the star’s orientation was drawn randomly from an isotropic distribution. Figure 6 shows σ_λ as a function of ψ for three illustrative values of the impact parameter, and for two choices of σ_v . The bias depends strongly on b , reflecting the limiting behaviors of Eqn 15: $\sigma_\lambda \propto \cos^2 \lambda$ as $b \rightarrow 0$, and $\sigma_\lambda \propto \sin^2 \lambda$ as $b \rightarrow 1$. The rightmost panel of Figure 6 shows that after marginalizing over a uniform distribution of b between 0 and 1, σ_λ varies weakly with ψ . Values of $\psi = 0^\circ$ and 180° lead to average values of σ_λ that are about two times lower than when $\psi = 90^\circ$. Thus, we expect that any such bias in the real sample to be small and to favor well-aligned and anti-aligned systems rather than producing a peak at $\psi = 90^\circ$.

7.3. The $v \sin i$ method

Many of the constraints on stellar inclination come from the combination of measurements of the star’s projected rotation velocity $v \sin i$, radius R , and rotation period P_{rot} , based on Equation 9. Any selection biases regarding R are unlikely to depend on the star’s orientation, but $v \sin i$ and P_{rot} are potentially problematic. Measurements of $v \sin i$ tend to be limited to an accuracy of $1\text{--}2 \text{ km s}^{-1}$ by systematic effects; thus, we would expect the fractional uncertainty in $v \sin i$ to be larger when $\sin i$ is small. Small values of $\sin i$ also make measurements of P_{rot} more difficult, because the photometric variability due to starspots and plagues has a lower amplitude at low inclinations.

We conducted more Monte Carlo trials to understand the consequent selection biases as a function of ψ . The intrinsic stellar properties were held fixed: $R = R_\odot$, $P_{\text{rot}} = 15$ days, and a maximum loss of light due to spots

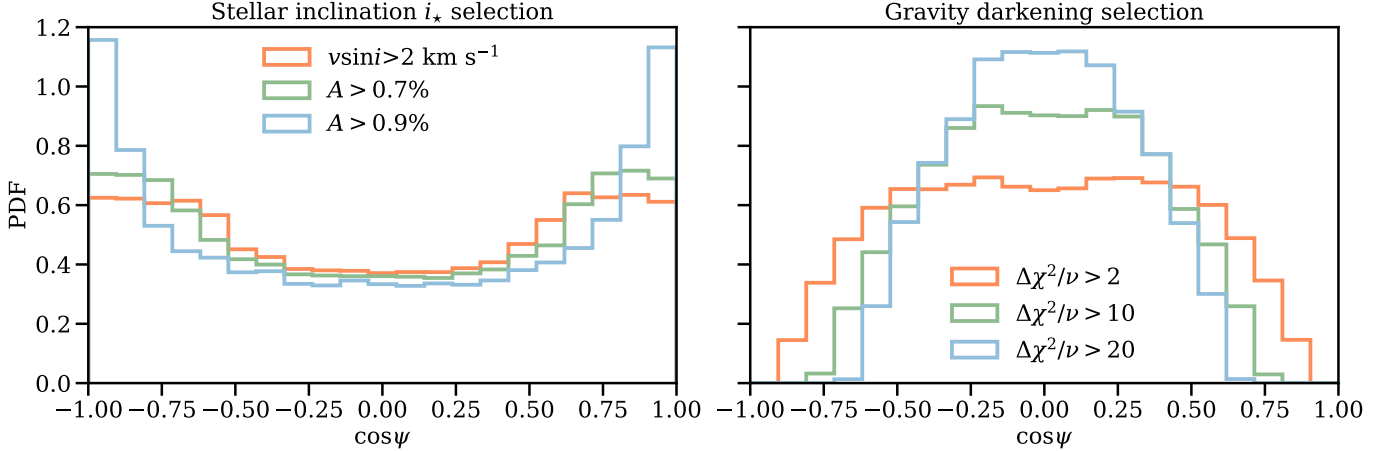


Figure 7. Biases in the $v \sin i$ method (Section 7.3) and the gravity darkening method (Section 7.4) shape the recovered obliquity distribution. Each panel shows the obliquity distribution of hypothetical stars drawn from a randomly-oriented population, after applying increasingly stringent detection thresholds. *Left:* Obliquities measured with the $v \sin i$ method, using three detection thresholds: (i) $v \sin i > 2 \text{ km s}^{-1}$, (ii) photometric amplitude $A > 0.7\%$, where $A = f_{\text{spot}} \sin i$, and (iii) $A > 0.9\%$. The $v \sin i$ method favors $\psi = 0^\circ$ and 180° . *Right:* Obliquities measured with the gravity-darkening method. The detection thresholds were parameterized by the difference in reduced- χ^2 between modeling the light curve with gravity-darkening or a standard transit profile.

of $f_{\text{spot}} = 1\%$. In each trial, the star’s orientation and the planet’s obliquity were drawn independently from an isotropic distribution. We assumed the photometric variability amplitude A to be $f_{\text{spot}} \sin i$, an approximation that assumes the spots are small and nearly equatorial, and neglects the effects of limb darkening (see, e.g., Jackson & Jeffries 2012; Mazeh et al. 2015). The stellar inclination was considered “measurable” when $v \sin i > 2 \text{ km s}^{-1}$ and $A > A_{\text{min}}$, or equivalently,

$$\sin i > \max \left[\frac{2 \text{ km s}^{-1}}{v}, \frac{A_{\text{min}}}{f_{\text{spot}}} \right]. \quad (16)$$

For the adopted stellar parameters, the $v \sin i$ criterion is the limiting factor when $A_{\text{min}} \lesssim 0.6\%$. Figure 7 shows the obliquity distribution of stars with measurable inclinations, for increasingly stringent detection criteria.

These selection effects would cause the sample to be biased in favor of well-aligned and anti-aligned systems, for which the inclination is guaranteed to be close to 90° . Misaligned systems, and perpendicular systems in particular, would occasionally be observed pole-on and are thereby disfavored.

7.4. Gravity Darkening

The photosphere of a rapidly rotating star is cooler and fainter near the equator than the poles, because the equatorial region is centrifugally lifted to higher elevation. This effect, known as gravity darkening, causes distortions of a transit light curve that depend on both λ and i_* in addition to the usual transit parameters (Barnes 2009). For five of the systems in the ψ sam-

ple (KELT-9, KELT-17, Kepler-13, MASCARA-4, and WASP-189), the stellar obliquity was determined by modeling transit light curves affected by gravity darkening. In contrast, none of the measurements in the λ sample relied on gravity darkening. Could this difference account for the differences in the inferred obliquity distributions of the ψ and λ samples?

Gravity-darkening anomalies in the light curve are typically on the order of $\lesssim 0.1\%$, making them challenging to detect, and the detectability depends on the stellar orientation. When ψ is near 0° or 180° , the transit light curve retains its usual “U-shape” with mirror symmetry around the time of minimum light, causing the parameters describing gravity darkening to be strongly covariant with the usual transit parameters. For other obliquities, the transit light curve develops an asymmetry or a “W-shape”, either of which reduces the covariance between the gravity-darkening parameters and the other parameters, allowing the gravity-darkening signal to be detected and interpreted with greater confidence. Thus, the sample of systems for which the gravity darkening signal has been reported is likely to be biased against well-aligned and anti-aligned systems.

To understand the extent of this bias, we performed another round of Monte Carlo trials involving a single star that can have any obliquity and a transiting planet that can have any impact parameter. Based on the properties of one of the best studied systems, Kepler-13A (Masuda 2015), we fixed the properties of the hypothetical star to be $M = 1.80 M_\odot$, $R = 1.71 R_\odot$, $P_{\text{rot}} = 20$ hours, $r/R = 0.085$, and $P_{\text{orb}} = 1.76$ days.

A quadratic limb-darkening law was adopted, with coefficients given by Masuda (2015): $u_1 + u_2 = 0.53$ and $u_1 - u_2 = 0.26$. The effective temperature T was assumed to vary with surface gravity g as

$$T = (7500 \text{ K}) \left(\frac{g}{g_{\text{pole}}} \right)^{1/4}. \quad (17)$$

In each of 2×10^5 trials, the stellar orientation was drawn from an isotropic distribution, and the planet’s transit impact parameter was drawn from a uniform distribution between 0 and 1. We generated a transit light curve exhibiting the effects of gravity darkening using the `pytransit` code written by Parviainen (2015). We calculated the difference in reduced- χ^2 between the best-fit model including gravity darkening and the best-fit model with no gravity darkening. For computational efficiency, only i_* , λ , P_{rot} , the limb-darkening coefficients, and r/R were treated as free parameters. Through these Monte Carlo trials, we mapped the relation between $\Delta\chi^2/\nu$ and ψ .

Figure 7 shows the obliquity distribution of those systems for which $\Delta\chi^2/\nu$ exceeds a threshold value. Results for three different choices of the threshold value are shown. Even for modest detection thresholds (i.e., $\Delta\chi^2/\nu > 2$), the obliquity distribution of the systems with detectable gravity-darkening signals is biased strongly against $\psi = 0^\circ$ and 180° .

The bias goes in the right direction to explain why the ψ sample shows stronger evidence for a “pile-up” of obliquities near 90° than the λ sample. To pursue this point, we repeated the modeling procedure described in Section 5 after excluding the 5 gravity-darkening systems from the sample. The resulting Bayes factors, relative to Model 1, are presented in the third row of Table 2. After omitting the gravity-darkening measurements, the ψ sample shows a weaker preference for a peak at 90° in the obliquity distribution. This trend is evident in Figure 5.

8. POPULATION SYNTHESIS

Bayesian analysis of the ψ and λ samples did not distinguish between a peaked or flat distribution for the misaligned systems. While this result held for both the ψ and λ samples—as well as the weak-tides sub-sample—minor discrepancies persist: the ψ sample marginally favors a 90° peak, more so than the λ sample, and the posteriors of the model parameters only partially overlap between the ψ and λ samples. Prompted by these mysteries, we investigated selection biases in Section 7.

However, the impacts of selection biases are difficult to constrain for heterogeneous samples. Stars with dif-

ferent characteristics may have different stellar obliquity distributions, and they may also have different characteristics that affect whether the stellar obliquity can be measured. For example, the ability to measure rotation periods from photometry is easier for cool spotted stars with convective envelopes than for hotter stars with radiative envelopes, and there is also evidence that cool and hot stars have intrinsically different obliquity distributions. We advocate for the creation of a more homogeneous sample to understand and overcome these biases. To achieve this goal, would it be better to focus on λ measurements, which are observationally expensive, or on $\sin i$ measurements, which bear less information but are less expensive?

We performed some Monte Carlo experiments to begin answering this question. We generated a synthetic sample of obliquities drawn from an isonormal model with $w = 0.7$, a level of “peakedness” motivated by the fits to the current sample. Host star properties and measurement uncertainties were assigned for each draw by randomly selecting host stars and their measurement uncertainties from the observed sample. This process neglected the dependence of σ_λ on λ and $\sigma_{v \sin i}$ on $v \sin i$, but retained the $v \sin i$ selection bias by enforcing realistic uncertainties $\sigma_{v \sin i}$. For a given synthetic sample, we computed the Bayes factor comparing the isonormal model and an isotropic model. The peaked distribution was deemed “recovered” if the Bayes factor for the isonormal model relative to the isotropic model was greater than 10. When calculating Bayes factors, we considered three scenarios: (i) measuring λ only, via the RM effect; (ii) measuring $\sin i$ only, by combining $v \sin i$, R_* , and P_{rot} ; and (iii) measuring both λ and $\sin i$ (the ψ sample). We did not consider gravity darkening measurements because of the strong bias of that method against aligned and anti-aligned stars. For a given choice of sample size and measurement technique, 500 trials were conducted.

Figure 8 shows the fraction of trials in which the peaked model was successfully recovered. To reach a success rate of $> 90\%$, the necessary sample size was 180, 200, and 1000, for the ψ , λ , and $\sin i$ samples, respectively. As expected from the results presented in Section 5.1, a single λ measurement is typically more valuable than a single $\sin i$ measurement. However, a typical RM measurement requires a time-critical observation lasting ≈ 5 hr on a large telescope with a stabilized high-resolution spectrograph. In contrast, measuring $v \sin i$ with such a telescope requires no more than 15 minutes (including overheads), does not require a highly stable wavelength calibration, and can be conducted at any time. Applying these fiducial costs of 5 hr per λ mea-

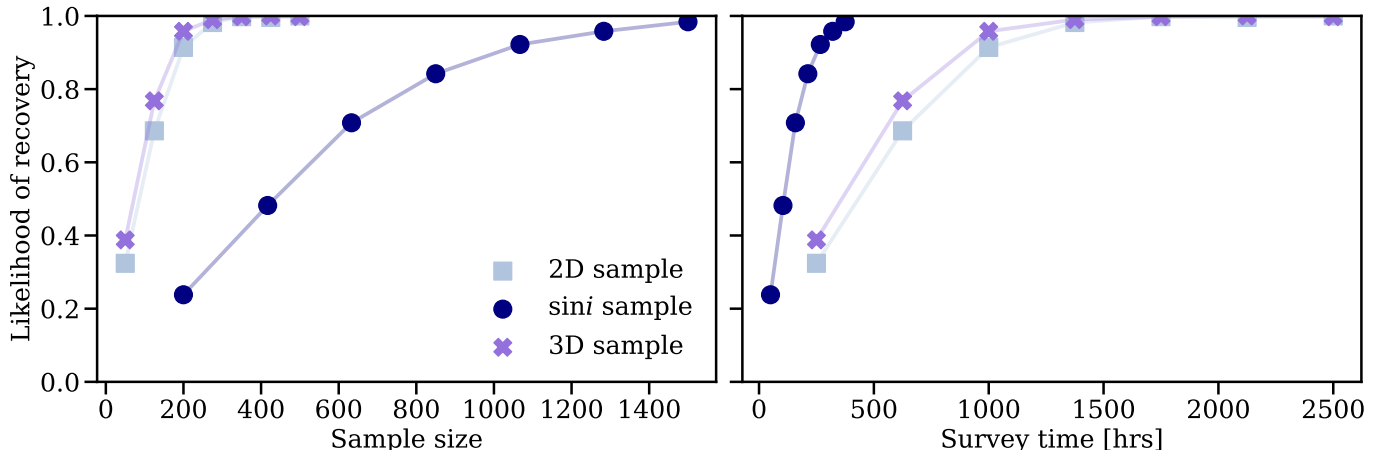


Figure 8. Observational investment required to recover a peaked obliquity distribution, for three idealized campaigns: (i) measuring λ only, (ii) measuring $\sin i$ only, and (iii) measuring both λ and $\sin i$. The vertical axis is the fraction of realizations in which the postulated peak (see text) is successfully identified. In the left panel, the horizontal axis is the sample size; in the right panel, the horizontal axis is the total observing time, assuming 5 hr per λ measurement and 0.25 hr per $\sin i$ measurement.

surement and 0.25 hr per $\sin i$ measurement, we found that the necessary observing time is 990, 980, and 250 hr for the ψ , λ , and $\sin i$ samples, respectively. Thus, in these simulations, the $v \sin i$ technique is favored, even without accounting for bad weather and scheduling constraints that would also favor the $v \sin i$ technique. Because of all the simplifying assumptions, these results should be considered illustrative rather than quantitatively reliable.

9. SUMMARY AND CONCLUSIONS

Even before the first misaligned planetary systems were discovered, theorists explored mechanisms for tilting a planet’s orbital plane away from the star’s equatorial plane (e.g., Yu & Tremaine 2001; Fabrycky & Tremaine 2007). Theoretical activity accelerated after the first few sightings of grossly misaligned systems (e.g., Hébrard et al. 2008; Winn et al. 2009; Queloz et al. 2010), leaving us with numerous proposed mechanisms for spin-orbit misalignment, such as magnetic warping of the protoplanetary disk (Foucart & Lai 2011), Von Zeipel–Kozai–Lidov cycles (Fabrycky & Tremaine 2007; Naoz et al. 2011), planet-planet scattering (Chatterjee et al. 2008), and inclination excitation from secular resonance crossing (Petrovich et al. 2020). Characterizing the observed obliquity distribution is an important goal in testing these theories for spin-orbit misalignment.

We applied hierarchical Bayesian inference to a sample of 174 planets (72 with full-obliquity constraints and 102 with only projected-obliquity constraints). Through Bayesian model selection, we tried to establish: (i) Is the obliquity distribution compatible with a single smooth distribution centered on 0° ? (ii) Are the misaligned systems consistent with isotropy or do they exhibit a con-

centration? (iii) If so, what is the preferred value of the obliquity?

A single Rayleigh distribution was found to be a terrible description of the data, relative to the models in which some systems are drawn from a Rayleigh distribution and others are drawn from a broader distribution. The sample with full-obliquity constraints showed greater evidence for a peak in the obliquity distribution at about 90° , relative to a model in which the misaligned systems are drawn from an isotropic distribution. However, the odds ratios were modest ($\lesssim 3$), and the results are likely affected by the selection bias of the gravity-darkening method that favors near-perpendicular systems. Analyzing the larger sample of systems with only projected-obliquity constraints, or the union of all systems with any kind of obliquity constraints, the Bayesian evidence did not reveal any preference for a concentration near 90° . Our investigation of selection biases showed that the gravity-darkening method favors systems with large obliquities, as noted above, while the other methods favor aligned and anti-aligned systems.

We believe that major progress on measuring the obliquity distribution will require the construction of a large sample of systems that have been measured with the same technique (or combination of techniques), coupled with a good understanding of the selection function. It is not clear how to achieve this goal. The RM technique is observationally expensive, typically requiring 4–5 hours per system using a large telescope equipped with a high-resolution spectrograph. The gravity-darkening technique requires transiting planets around rapidly rotating stars, of which few are known; it also requires very precise transit photometry. The $v \sin i$ technique is the

only one for which it seems feasible to expand the sample to thousands of stars or more. Only a single high-resolution spectrum of each system is needed, along with the stellar rotation period, which can be obtained from ongoing or planned wide-field photometric time-domain surveys. The ideal types of star are probably early G stars or late F stars, for which moderately rapid rotation is expected ($\gtrsim 5$ km/s) and for which rotationally-induced photometric variations are also expected. Our population-synthesis calculations demonstrated that a $v \sin i$ survey would require less observing time than a RM survey (by a factor of a few) to distinguish between a peaked and isotropic obliquity distribution, although these calculations were based on many simplifying assumptions. Before deciding on an observing program, other considerations would need to be taken into account, such as the availability and reliability of photometric rotation periods, and the limited number of transiting planets that are known to exist around early

G and late F stars. Nobody said that solving the spin-orbit misalignment problem would be easy.

ACKNOWLEDGMENTS

We thank Jiayin Dong and Dan Foreman-Mackey for helpful conversations and for sharing their preprint of a paper about modeling the obliquity distribution. JS acknowledges support by the National Science Foundation Graduate Research Fellowship Program under Grant DGE-2039656. SHA acknowledges the hospitality of the Department of Astrophysical Sciences at Princeton University and support from the Danish Council for Independent Research through a grant, No. 2032-00230B. Any opinions, findings, and conclusions or recommendations expressed in this material are those of the author(s) and do not necessarily reflect the views of the National Science Foundation.

REFERENCES

- Abbott, T. M. C., Abdalla, F. B., Alarcon, A., et al. 2018, *PhRvD*, 98, 043526, doi: [10.1103/PhysRevD.98.043526](https://doi.org/10.1103/PhysRevD.98.043526)
- Albrecht, S., Winn, J. N., Johnson, J. A., et al. 2012, *ApJ*, 757, 18, doi: [10.1088/0004-637X/757/1/18](https://doi.org/10.1088/0004-637X/757/1/18)
- Albrecht, S. H., Dawson, R. I., & Winn, J. N. 2022, *PASP*, 134, 082001, doi: [10.1088/1538-3873/ac6c09](https://doi.org/10.1088/1538-3873/ac6c09)
- Albrecht, S. H., Marcussen, M. L., Winn, J. N., Dawson, R. I., & Knudstrup, E. 2021, *ApJL*, 916, L1, doi: [10.3847/2041-8213/ac0f03](https://doi.org/10.3847/2041-8213/ac0f03)
- Barnes, J. W. 2009, *ApJ*, 705, 683, doi: [10.1088/0004-637X/705/1/683](https://doi.org/10.1088/0004-637X/705/1/683)
- Bourrier, V., Lovis, C., Cretignier, M., et al. 2021, *A&A*, 654, A152, doi: [10.1051/0004-6361/202141527](https://doi.org/10.1051/0004-6361/202141527)
- Bourrier, V., Attia, O., Mallonn, M., et al. 2023, *A&A*, 669, A63, doi: [10.1051/0004-6361/202245004](https://doi.org/10.1051/0004-6361/202245004)
- Chatterjee, S., Ford, E. B., Matsumura, S., & Rasio, F. A. 2008, *ApJ*, 686, 580, doi: [10.1086/590227](https://doi.org/10.1086/590227)
- Fabrycky, D., & Tremaine, S. 2007, *ApJ*, 669, 1298, doi: [10.1086/521702](https://doi.org/10.1086/521702)
- Fabrycky, D. C., & Winn, J. N. 2009, *ApJ*, 696, 1230, doi: [10.1088/0004-637X/696/2/1230](https://doi.org/10.1088/0004-637X/696/2/1230)
- Foucart, F., & Lai, D. 2011, *MNRAS*, 412, 2799, doi: [10.1111/j.1365-2966.2010.18176.x](https://doi.org/10.1111/j.1365-2966.2010.18176.x)
- Frazier, R. C., Stefansson, G., Mahadevan, S., et al. 2022, arXiv e-prints, arXiv:2212.06266, doi: [10.48550/arXiv.2212.06266](https://doi.org/10.48550/arXiv.2212.06266)
- Gaudi, B. S., & Winn, J. N. 2007, *ApJ*, 655, 550, doi: [10.1086/509910](https://doi.org/10.1086/509910)
- Grouffal, S., Santerne, A., Bourrier, V., et al. 2022, *A&A*, 668, A172, doi: [10.1051/0004-6361/202244182](https://doi.org/10.1051/0004-6361/202244182)
- Hébrard, G., Bouchy, F., Pont, F., et al. 2008, *A&A*, 488, 763, doi: [10.1051/0004-6361:200810056](https://doi.org/10.1051/0004-6361:200810056)
- Hjorth, M., Albrecht, S., Hirano, T., et al. 2021, *Proceedings of the National Academy of Science*, 118, e2017418118, doi: [10.1073/pnas.2017418118](https://doi.org/10.1073/pnas.2017418118)
- Hogg, D. W., Myers, A. D., & Bovy, J. 2010, *ApJ*, 725, 2166, doi: [10.1088/0004-637X/725/2/2166](https://doi.org/10.1088/0004-637X/725/2/2166)
- Jackson, R. J., & Jeffries, R. D. 2012, *MNRAS*, 423, 2966, doi: [10.1111/j.1365-2966.2012.21119.x](https://doi.org/10.1111/j.1365-2966.2012.21119.x)
- Knudstrup, E., Albrecht, S. H., Gandolfi, D., et al. 2023, arXiv e-prints, arXiv:2302.01702, doi: [10.48550/arXiv.2302.01702](https://doi.org/10.48550/arXiv.2302.01702)
- Louden, E. M., Winn, J. N., Petigura, E. A., et al. 2021, *AJ*, 161, 68, doi: [10.3847/1538-3881/abcebd](https://doi.org/10.3847/1538-3881/abcebd)
- Masuda, K. 2015, *ApJ*, 805, 28, doi: [10.1088/0004-637X/805/1/28](https://doi.org/10.1088/0004-637X/805/1/28)
- Masuda, K., & Winn, J. N. 2020, *AJ*, 159, 81, doi: [10.3847/1538-3881/ab65be](https://doi.org/10.3847/1538-3881/ab65be)
- Mazeh, T., Perets, H. B., McQuillan, A., & Goldstein, E. S. 2015, *ApJ*, 801, 3, doi: [10.1088/0004-637X/801/1/3](https://doi.org/10.1088/0004-637X/801/1/3)
- Morton, T. D., & Winn, J. N. 2014, *ApJ*, 796, 47, doi: [10.1088/0004-637X/796/1/47](https://doi.org/10.1088/0004-637X/796/1/47)
- Mounzer, D., Lovis, C., Seidel, J. V., et al. 2022, *A&A*, 668, A1, doi: [10.1051/0004-6361/202243998](https://doi.org/10.1051/0004-6361/202243998)
- Muñoz, D. J., & Perets, H. B. 2018, *AJ*, 156, 253, doi: [10.3847/1538-3881/aae7d0](https://doi.org/10.3847/1538-3881/aae7d0)

- Naoz, S., Farr, W. M., Lithwick, Y., Rasio, F. A., & Teyssandier, J. 2011, *Nature*, 473, 187, doi: [10.1038/nature10076](https://doi.org/10.1038/nature10076)
- Parviainen, H. 2015, *MNRAS*, 450, 3233, doi: [10.1093/mnras/stv894](https://doi.org/10.1093/mnras/stv894)
- Petrovich, C., Muñoz, D. J., Kratter, K. M., & Malhotra, R. 2020, *ApJL*, 902, L5, doi: [10.3847/2041-8213/abb952](https://doi.org/10.3847/2041-8213/abb952)
- Queloz, D., Anderson, D. R., Collier Cameron, A., et al. 2010, *A&A*, 517, L1, doi: [10.1051/0004-6361/201014768](https://doi.org/10.1051/0004-6361/201014768)
- Rice, M., Wang, S., Gerbig, K., et al. 2023, *AJ*, 165, 65, doi: [10.3847/1538-3881/aca88e](https://doi.org/10.3847/1538-3881/aca88e)
- Rice, M., Wang, S., Wang, X.-Y., et al. 2022, *AJ*, 164, 104, doi: [10.3847/1538-3881/ac8153](https://doi.org/10.3847/1538-3881/ac8153)
- Triaud, A. H. M. J. 2018, in *Handbook of Exoplanets*, ed. H. J. Deeg & J. A. Belmonte, 2, doi: [10.1007/978-3-319-55333-7_2](https://doi.org/10.1007/978-3-319-55333-7_2)
- Trotta, R. 2007, *MNRAS*, 378, 72, doi: [10.1111/j.1365-2966.2007.11738.x](https://doi.org/10.1111/j.1365-2966.2007.11738.x)
- Winn, J. N., Fabrycky, D., Albrecht, S., & Johnson, J. A. 2010, *ApJL*, 718, L145, doi: [10.1088/2041-8205/718/2/L145](https://doi.org/10.1088/2041-8205/718/2/L145)
- Winn, J. N., Johnson, J. A., Fabrycky, D., et al. 2009, *ApJ*, 700, 302, doi: [10.1088/0004-637X/700/1/302](https://doi.org/10.1088/0004-637X/700/1/302)
- Winn, J. N., Petigura, E. A., Morton, T. D., et al. 2017, *AJ*, 154, 270, doi: [10.3847/1538-3881/aa93e3](https://doi.org/10.3847/1538-3881/aa93e3)
- Yu, Q., & Tremaine, S. 2001, *AJ*, 121, 1736, doi: [10.1086/319401](https://doi.org/10.1086/319401)
- Zhao, L. L., Kunovac, V., Brewer, J. M., et al. 2022, *Nature Astronomy*, doi: [10.1038/s41550-022-01837-2](https://doi.org/10.1038/s41550-022-01837-2)